Batteries & Supercaps

Chemistry Europe
European Chemical Societies Publishing

Batteries & Supercaps

RESEARCH ARTICLE OPEN ACCESS

Electrolyte-Dependent Aging Analysis in SiO_x-Based Li-Ion Batteries via Composite Electrode Model

Mitsunori Nakamoto[1] | Benoit Mathieu[2] | Khawla Zrikem[2] | Masato Yano[1] | Masatomo Tanaka[1] | Irina Profatilova[2] | Hideyuki Kumita[1] | Anass Benayad[3] | Ambroise Van Roekeghem[2]

[1]Murata Manufacturing Co., Ltd., Nagaokakyo-shi, Kyoto, Japan | [2]Université Grenoble Alpes, CEA, LITEN, Grenoble, France | [3]Institute for Applied Materials-Energy Storage System, Karlsruhe Institute of Technology, Eggenstein-Leopoldshafen, Germany

Correspondence: Mitsunori Nakamoto (mitsunori.nakamoto@murata.com) | Ambroise Van Roekeghem (ambroise.vanroekeghem@cea.fr)

Received: 18 February 2026 | **Revised:** 4 June 2026 | **Accepted:** 16 June 2026

Keywords: cycle aging | lithium-ion battery | pseudo-two-dimensional model | SiO_x anode | solid-electrolyte interphase

ABSTRACT

The performance of lithium-ion batteries with silicon oxide (SiO_x) is influenced by solid electrolyte interphase (SEI) formation and associated lithium consumption. This study investigates the role of electrolyte composition in governing SEI evolution, lithium consumption, and aging behaviors in $LiCoO_2$|SiOx cells using complementary experimental and modeling approaches. Electrolytes containing fluoroethylene carbonate (FEC) exhibit significantly improved cycle retention compared with conventional ethylene carbonate (EC)-based electrolytes. Nuclear magnetic resonance spectroscopy reveals two distinct SEI formation pathways: EC decomposition yields an organic-rich SEI, whereas FEC and PF_6^- decomposition produce an inorganic, LiF-rich SEI. The total SEI mass remains nearly constant after aging, indicating dynamic breathing behavior rather than continuous growth. Based on these insights, we developed a pseudo-two-dimensional model that couples electrolyte consumption and SEI growth by distinguishing organic and inorganic SEI components with different mechanical responses to SiO_x volume changes. The model successfully predicts electrolyte-dependent aging, reproducing the influence of FEC concentration on overpotential, loss of lithium inventory, and capacity fade. The rate performance of the cell is primarily limited by lithium transport within SiO_x particles and by electrolyte transport across the electrode, particularly under fast-charging conditions. Our combined experimental-modeling approach provides a foundation for electrolyte-specific aging assessment and electrolyte design for SiO_x-based batteries.

1 | Introduction

Lithium-ion batteries (LIBs) are one of the indispensable devices in modern life. However, higher energy density is demanded for some applications such as electric vehicles and electric aircraft [1–3]. One promising approach to improve the energy density is to adopt silicon-based active materials as a negative electrode. In particular, the family of silicon oxide (SiO_x) materials is seen as a promising candidate, demonstrating a lower energy density at the beginning of life but enhanced cycle life compared with pure silicon anodes [4–7]. However, typical SiO_x materials are subject to large volume changes during lithiation and delithiation processes, which could lead to the cracking of SiO_x particles or to the disconnection of electric paths between SiO_x particles. To fully leverage the potential of SiO_x anodes, it is necessary to gain deeper insight into the aging processes of SiO_x in a battery cell.

It is well-known that the nature and proportion of electrolyte constituents strongly affect the degree of degradation in aging tests, especially for SiO_x-based cells. Many studies have concluded that the inclusion of fluoroethylene carbonate (FEC) results in enhanced cycle life of the cells [8, 9]. When FEC is incorporated into the electrolyte, the solid electrolyte interphase (SEI), the surface film formed at the interface between the anode active material and the electrolyte, is likely to have desirable properties [10, 11]. However, the details of SEI growth during

cycle aging and the direct correlation of the SEI nature to cell performance are missing in the literature.

In recent years, several studies have reported the development of pseudo-two-dimensional (P2D) models [12–15] with some degradation modes such as loss of active materials, loss of lithium inventory (LLI), and SEI growth [16–19]. P2D models, also referred to as Doyle-Fuller-Newman models, are widely acknowledged for a good balance between accuracy, flexibility, and computational speed. Specifically, SEI models have been implemented in P2D models, and such P2D-based SEI models [16, 20, 21] mainly describe capacity fade using single-layer or effective SEI growth kinetics without explicitly considering electrolyte-dependent SEI chemistry. More advanced porous or multilayer SEI frameworks [22–25] primarily focused on transport phenomena and SEI morphology evolution, while direct coupling between experimentally identified SEI composition, electrolyte formulation, and electrochemical degradation behavior remained limited, especially for SiO_x-based electrodes.

In this work, we develop a physics-based P2D model that explicitly couples electrolyte consumption and SEI growth in SiO_x-based negative electrodes, where the anode active material consists of 100% SiO_x. The model distinguishes two SEI components, an inorganic phase and an organic phase, and assigns phase-specific behaviors during lithiation and delithiation of SiO_x. A systematic comparison between modeling and experimental results is performed, where our experiment combines electrochemical measurements with detailed SEI characterization by nuclear magnetic resonance (NMR). This integrated experimental-modeling approach provides insight into how electrolyte composition governs the competition between multiple SEI formation pathways and the resulting diversity of SEI species. Furthermore, the model incorporates recurring SEI damage induced by the large volume changes of SiO_x during cycling, leading to continuous consumption of electrolyte solvents and lithium ions. After calibration, the framework enables the reproduction of electrolyte-dependent aging behaviors, notably capturing the impact of FEC concentration on long-term cycling performance. The complementary modeling and experimental approaches yield a deeper and more accurate understanding of aging mechanisms in SiO_x negative electrodes and their dependence on electrolyte formulation. Degradation in SiO_x-based electrodes generally involves multiple coupled phenomena, including electrolyte-derived SEI formation, irreversible lithiation of oxygen-containing SiO_x matrices, lithium trapping, and transport limitations associated with the evolving interphase [5, 26, 27]. In the present work, we specifically focus on the electrolyte-dependent contribution to degradation, namely the relationship between SEI chemistry, lithium consumption, and electrochemical performance in SiO_x-based cells. Accordingly, we adopt a reduced representation of the SEI based on two dominant components, aiming to capture the essential electrolyte-dependent degradation trends.

2 | Method

2.1 | Electrochemical Measurements

We consider pouch cells with $LiCoO_2$ (LCO) [28] as a cathode active material and amorphous SiO_x as an anode active material, in which the Si:O ratio is around 1:1.1. The positive electrode is composed of LCO (97.2 wt%), Ketjenblack (1.2 wt%), and polyvinylidene difluoride (1.6 wt%), while the negative electrode is composed of SiO_x (80.0 wt%), acetylene black (4.0 wt%), vapor grown carbon fiber (1.0 wt%), and polyimide binder (15.0 wt%). The diameters of positive and negative electrodes are 16.5 and 17.0 mm, respectively. The loadings of positive and negative electrodes are 21.05 and 1.74 mg/cm^2, respectively, excluding current collectors. Average active material particle diameters are 20.5 and 5.9 μm for positive and negative electrodes.

LCO was selected as a model cathode active material due to its well-defined electrochemical behavior and relatively limited parasitic reactions [28], enabling us to focus on degradation mechanisms at the SiO_x negative electrode. The key mechanisms discussed in this work are expected to remain qualitatively valid in the systems with Ni-rich cathodes, even though additional factors such as transition metal dissolution and electrolyte oxidation may affect SEI evolution with Ni-rich cathodes [29].

Open-circuit voltage (OCV) curves as a function of lithium content were represented by the potential curves in SiO_x half cells cycled under 0.01/0.01 C conditions. The OCV for SiO_x has a hysteresis between the lithiation and delithiation stages. We measured the lithiation OCV and the delithiation OCV separately, and they are independently applied to the charge/discharge process in the model.

Cycle aging tests were conducted under 0.5/0.5 C conditions, where charging was carried out in CC/CV mode with the potential cutoff of 4.3 V, while discharging was carried out in CC mode with the potential cutoff of 3.0 V. A rest time of 10 min was inserted after every charge and discharge. In the cycle tests, three loading tests were inserted at 1,116, and 178 cycles. Each loading test, named as first, second, and third loading test, consists of 10 charge/discharge steps. The first five charge/discharge cycles were conducted at the discharging rates of 0.1, 0.2, 0.5, 1.0, and 2.0 C with the constant charging rate of 0.1 C. The following five cycles were performed at the charging rates of 0.1, 0.2, 0.5, 1.0, and 2.0 C with the constant discharging rate of 0.1 C. The aging test was initiated with 0.5/0.5 C (cycle 0), whose discharge capacity is the standard for the capacity retention in later cycles.

We developed a pouch cell with a small piece (approximately 1 mm × 1 mm) of $LiFePO_4$ (LFP) reference electrode inserted between the positive and negative electrodes without direct contact between them [30]. LFP had been partially delithiated in advance so that its State of Charge (SOC) is located at the flat region of its OCV potential. Even though the reference-electrode measurements may be affected by local electrolyte polarization, current distribution, and reference-electrode stability, particularly during long-term cycling [30], this configuration provides not only the cell voltage but also the positive electrode potential and the negative electrode potential separately. The potentials were converted by assuming that the potential of the LFP plateau is 3.4 V versus Li/Li$^+$.

In this work, we compared the electrochemical performances of two systems with different electrolyte compositions. One electrolyte is 1 M $LiPF_6$/EC + DMC (EC:DMC = 15:85 wt%), denoted as the EC + DMC system, the other is 1 M $LiPF_6$/DMC + FEC

(DMC:FEC = 85:15 wt%), denoted as the DMC + FEC system, where EC and DMC stand for ethylene carbonate (EC) and dimethyl carbonate, respectively. These experimental results were used for the model calibration. Other cycle tests for additional systems of 1 M $LiPF_6$/EC + DMC + FEC with varied FEC ratios were experimentally measured and are discussed in the context of model validation. All the measurements in this article were carried out at 23 °C with the pouch cell pressurized under 0.7 MPa perpendicular to the cell plane.

2.2 | SEI Characterization and Quantification by NMR

SEI generated on the SiO_x electrode surface after charge–discharge cycles was experimentally characterized and quantified. To this end, three cells were dismantled after discharging, and the extracted negative electrodes were rinsed with DMC to remove residual electrolyte and dried. All NMR samples were prepared by D_2O extraction from the negative electrode. ^1H and ^{19}F NMR analyses were applied to the D_2O solutions, including the extracted SEI, using a Bruker Avance NEO 500 MHz NMR spectrometer, which enables the identification of key molecules respectively generated by relevant electrochemical reactions of the electrolyte solution. Organic SEI species derived from organic solvents were measured by ^1H NMR, whereas LiF was measured by ^{19}F NMR.

The organic SEI species experience hydrolysis reactions during the extraction process by D_2O [31]. For example, lithium ethyl carbonate (LEC) is converted to ethanol during the extraction process. The ethanol was detected and quantified by NMR, and we assume that the same molar amount of LEC was in the cell before the extraction. The correspondence between hydrolysis reactants and products is shown in Table 1. These potential products are complementarily rationalized by X-ray photoemission spectroscopy (XPS) analyses on negative electrode surfaces as discussed in Supporting Information S1. A few other minor organic molecules were also detected in our NMR measurements, but they accounted for less than 6% of the total SEI mass and are ignored for simplicity. In addition, other inorganic species frequently reported in the literature, such as Li_2CO_3, Li_2O, and lithium silicates, were not quantitatively resolved in the present NMR analysis and are therefore not explicitly included in the model discussed below. We hypothesize that these unresolved species contribute only marginally to the overall SEI mass in the investigated systems. The reaction mechanisms that lead to the generation of such SEI components have been previously reported using quantum chemical calculations [32–34]. These studies have shown that LEC mainly comes from one-electron reduction of EC and that dilithium ethylene dicarbonate (LEDC) is generated by the dimerization of LEC. It was also discussed that lithium methyl carbonate (LMC) originates from DMC, and LiF originates from FEC and $LiPF_6$. The detection of lithium formate (LF) in D_2O extraction is likely attributable to two possible origins involving in situ electrochemical formation and ex situ hydrolytic artifacts [35–37]. Primarily, LF is generated during battery operation via the electrochemical reduction of CO_2, a byproduct of electrolyte decomposition. CO_2 is scavenged by surface protons or hydride species at the reductive anode interface, stabilizing as formate. Concurrently, the hydrolytic instability of organic SEI components contributes to the observed signal. Upon contact with D_2O, metastable species such as lithium alkyl carbonates or radical intermediates may undergo hydrolysis, releasing CO_2 or reactive fragments that rapidly convert to formate in the extraction medium. In order to estimate the composition of the SEI, the extraction and analysis of the SEI were conducted after the first cycle and at the cycle where the capacity retention becomes 80%.

Details of NMR measurements and their post analyses are discussed in Supporting Information S2.

TABLE 1 | Relationship between possible organic SEI components and the products directly detected by NMR measurements. The detected products are generated via hydrolysis of SEI components during the extraction process [31].

Observed molecule	Suggested SEI product	
Molecule after hydrolysis	**Molecule before hydrolysis**	**Molar mass, g/mol**
Formic acid	Lithium formate (LF)	51.96
Ethylene glycol	Dilithium ethylene dicarbonate (LEDC)	161.94
Ethanol	Lithium ethyl carbonate (LEC)	96.00
Methanol	Lithium methyl carbonate (LMC)	81.98

3 | Results and Discussion

3.1 | Experimental Results

Figure 1 displays the experimentally measured discharge capacity retention for the cells with two different electrolytes. It is clear

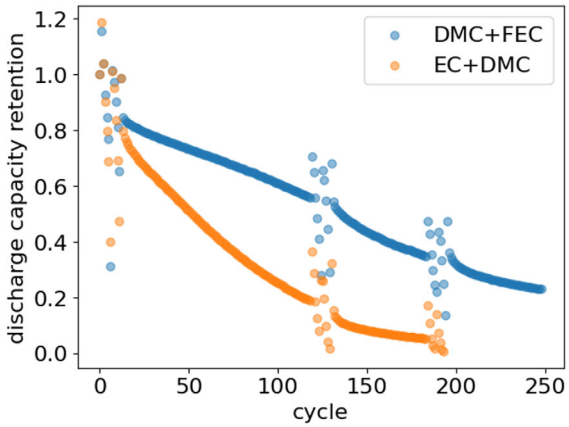

FIGURE 1 | Discharge capacity retention in experimental cycle aging tests for LCO|SiO_x cells with two distinct electrolytes: EC + DMC and DMC + FEC. Three loading tests are inserted at 1, 116, and 178 cycles. The cycle tests were carried out at 0.5/0.5 C conditions except for the loading tests. The test was initiated with 0.5/0.5 C (cycle 0), which is the standard for discharge capacity retention in later cycles.

that DMC + FEC exceeds EC + DMC in terms of cycle performance. The origin of the difference in capacity retention induced by the different electrolytes will be further discussed hereafter.

To quantify the constituents of the SEI film formed on the anode surface, these compounds were extracted using D_2O. During the D_2O extraction, the major organic components constituting the SEI film undergo hydrolysis reactions. According to the ^1H NMR spectrum, the signals were observed as a singlet at 3.67 ppm, a singlet at 3.36 ppm, a triplet at 1.19 ppm, and a singlet at 8.46 ppm, corresponding to ethylene glycol, methanol, ethanol, and formic acid, respectively. These directly observed hydrolysis products were finally attributed to the original SEI species, like LEC and LEDC [31], as shown in Table 1. Additionally, the ^{19}F NMR spectrum showed a singlet signal originating from LiF observed at approximately −120 ppm. The present NMR approach with D_2O extraction mainly detects hydrolyzable and soluble SEI species. Therefore, insoluble oligomeric or polymeric species potentially generated from FEC decomposition [38] may be difficult to detect if they do not hydrolyze or dissolve during the extraction process. In our supplementary investigations using model electrolytes with higher FEC contents (>50%), weak signals potentially attributable to polyethylene oxide-type oligomeric species were observed in the ^1H NMR spectra. However, such signals were not clearly detected for electrolyte compositions containing less than 50% of FEC, including the DMC + FEC electrolyte investigated in this study. This suggests that polymeric species are unlikely to constitute a dominant fraction of the SEI under the present conditions.

Figure 2 shows the amount of SEI film formed on the SiO_x anode, based on the quantities of detected hydrolysis products of organic SEI components and LiF extracted after the first cycle and after aging. LEC was detected in both electrolyte systems, which suggests that LEC may originate not only from EC but also from FEC when F is removed in one-electron reduction. LF was also observed in both electrolyte systems; we ascribe its formation to an artifact from the D_2O extraction process [35–37]. A slightly larger amount of LF in DMC + FEC seems consistent with the insight that FEC is likely to produce CO_2 in the reduction process [34]. In this work, we mainly focus on the degradation of EC and FEC, and emphasize the following aspects.

First, the most significant difference between EC + DMC and DMC + FEC systems comes from LEDC and LiF. Since LEDC was produced only in EC + DMC, LEDC is derived predominantly from EC. LiF was apparently rich in DMC + FEC, so FEC was the main source of LiF. The LiF-rich SEI reportedly has a desirable passivation capability [10]. We suppose that this improved passivation in DMC + FEC suppressed the formation of LMC, which originates from DMC occupying the largest part (85%) of electrolyte composition. The improvement was also qualitatively confirmed in our cycle aging test (Figure 1).

The present NMR results identify LiF as the most distinctive inorganic product in the FEC-containing electrolyte, whereas LEDC is characteristic of the EC-containing electrolyte. This interpretation is consistent with previous NMR-based studies on Si electrodes showing that FEC has an impact on the SEI chemical composition [11]; however, those studies also indicate that FEC can generate branched ethylene-oxide-based polymeric species in addition to LiF-rich inorganic products. Therefore, the LiF-rich SEI discussed here should be regarded as the experimentally measurable inorganic signature of FEC-derived passivation, while insoluble or weakly hydrolyzable polymeric species may be underestimated by the present D_2O-extraction protocol. This limitation justifies the use of LiF and LEDC as representative components for modeling, rather than as a complete molecular inventory of the SEI.

Second, the total amount of SEI was smaller in DMC + FEC compared to EC + DMC, both before and after aging. It has been reported that LiF-rich SEI leads to a compact film and is a key to suppressing capacity fades during cycle aging [39, 40].

Lastly, there is no significant change in the total amount of SEI at the beginning of life and after aging when each cell has lost 20% of its initial capacity, as shown in Figure 2. One hypothesis is that the electrode is maintained stably through the aging test; however, this is unlikely because SiO_x is subject to large volume changes. We might consider the "breathing" behavior of the film, whereby the film thickens during charging and contracts during discharging. This phenomenon was previously observed by our group using X-ray reflectivity measurements on thin SiO_x films [41]. Previous studies [42–44] have also reported dynamic

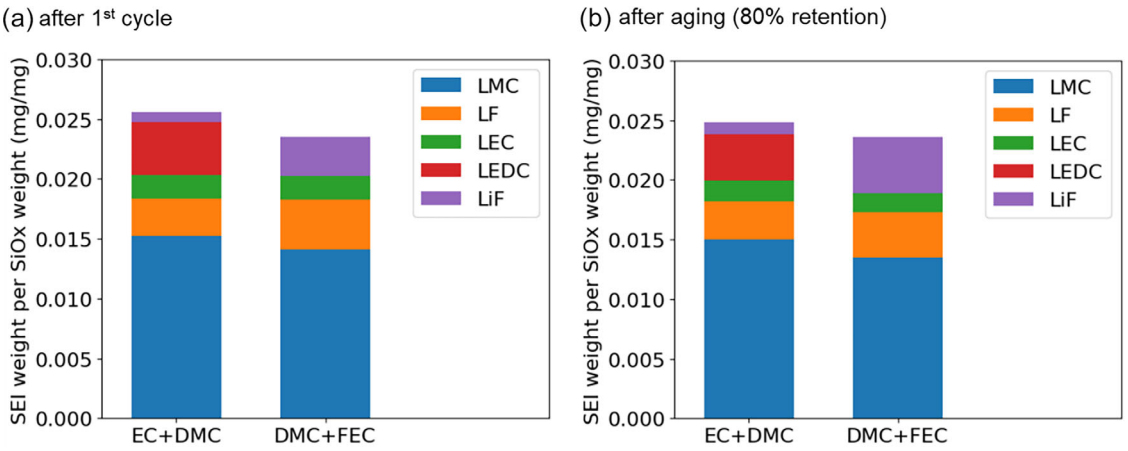

FIGURE 2 | The quantity of each SEI species extracted from the negative electrodes of dismantled cells and quantified by ^1H NMR and ^{19}F NMR. (a) After the first cycle. (b) At the cycle when discharge capacity retention becomes 80%.

changes in both the thickness and chemical composition of the SEI during electrochemical cycling. This behavior has been directly observed using operando techniques such as neutron reflectometry and has also been inferred from depth profiling and spectroscopic analyses. Reversible changes in SEI thickness have been correlated with variations in its chemical composition, particularly the formation and decomposition of carbonate species. Importantly, the apparent thinning of the SEI during delithiation has been attributed to multiple mechanisms. These include (i) electrochemical decomposition or re-oxidation of SEI components such as carbonate species, leading to partial removal of the interphase, and (ii) dissolution of organic SEI constituents into the electrolyte, resulting in a loss of material from the surface. In contrast, more stable inorganic components tend to remain on the electrode, contributing to the residual interphase. In this article, we rely on the hypothesis of a breathing SEI to develop an electrochemical model. The insights obtained by NMR analyses are well aligned with our XPS analyses for the negative electrode surface (Supporting Information S1).

In our preliminary calendar-aging experiments, degradation was limited compared to that observed during cycle aging, with only a weak dependency on electrolyte composition. This observation suggests that degradation in the present system is predominantly driven by cycling-induced processes rather than by storage-induced aging, which also supports the validity of the breathing SEI model.

3.2 | Modeling

3.2.1 | Modeling Framework and Assumptions

In order to interpret how the different electrolyte compositions influence cycle aging in the cells with SiO_x, we developed a P2D model augmented with electrolyte consumption and SEI growth modes. In contrast to conventional P2D-SEI models [16, 20, 21], where SEI growth is generally represented by a single effective layer or simplified kinetics, the present model explicitly distinguishes chemically different SEI components identified experimentally by NMR analyses. In particular, EC-derived organic SEI species are separated from FEC/PF_6-derived inorganic LiF-rich SEI, allowing electrolyte-dependent SEI chemistry to directly influence transport resistance, lithium consumption, and degradation behavior. The properties of each cell component, which reflect our experimental cells, are summarized in Table 2. The lithium insertion kinetics in the negative electrode have first been calibrated from experimental pulse tests, using very short pulses at different SOC, followed by a parametric study to reproduce the pulse overpotential and fit the parameters in the model. The diffusion coefficient in the anode active material has then been calibrated using 1 min pulse tests with the P2D model, using the calibrated insertion kinetics. It has been found that the stoichiometry dependency of diffusivity and insertion kinetics is similar. Therefore, we adopted a common stoichiometry dependency between them as described in Table 2. The detail is discussed in Supporting Information S3. A stoichiometry-dependent Li diffusivity has been reported for silicon materials, where Li diffusivity exhibits an increasing trend as lithiation proceeds, in a previous work [45].

TABLE 2 | Parameters based on experimental measurements. P, N, and S stand for positive electrode, negative electrode, and separator, respectively. Electrolyte parameters (ionic conductivity, diffusion constants, and transference numbers) are not shown here, but they are based on experimental data.

Parameter	Value
P | porosity	0.173
P | tortuosity	5.6
P | electronic conductivity	0.18 S/m
P | Li diffusivity in LCO	$1.7 \times 10^{-13}\ m^2/s$
P | insertion kinetics	$8.0 \times 10^{-6}\ A{\cdot}m^2{\cdot}(m^3{\cdot}mol)^{1.5}$
N | porosity	0.329
N | tortuosity	10.5
N | electronic conductivity	215 S/m
N | Li diffusivity in SiO_x	$D_0\left\{\frac{1}{0.005208 * \exp\left(\frac{1}{x^2}\right) + 1.1} + 0.1\right\}$ where $D_0 = 1.74 \times 10^{-15}\ m^2/s$ and x is the stoichiometry
N | insertion kinetics	$i_0\left\{\frac{1}{0.005208 * \exp\left(\frac{1}{x^2}\right) + 1.1} + 0.1\right\}$ where $i_0 = 6.5 \times 10^{-7}\ A{\cdot}m^2{\cdot}(m^3{\cdot}mol)^{1.5}$ and x is the stoichiometry
S | porosity	0.55
S | McMullin number	3

Our model is based on the porous SEI model assumption, where reactants in the electrolyte diffuse through the pores in the SEI, and they react at the surface of the active materials after accepting one or more electrons, giving rise to the products, which result in the formation and growth of SEI [24, 25]. In the previous section, we found that two SEI components, LiF and LEDC, are the main differences between the two electrolytes, thus determining the cell performance. It was reported that LiF produces a dense and brittle SEI layer, while LEDC gives a relatively sparse and flexible SEI layer [46, 47]. Following the given insights, we modeled the SEI with two entities, LiF and LEDC (a binary SEI). This simplification is supported by our NMR analysis, which indicates that LEDC and LiF are the primary contributors distinguishing the two electrolyte systems, while other identified species account for less than approximately 6% of the total SEI mass, except LMC. Therefore, LEDC and LiF can be regarded as representative components capturing the dominant organic and inorganic contributions governing electrolyte-dependent behavior. We emphasize that the objective of the present model is not to reproduce the full chemical composition of the SEI, but rather to describe the impact of electrolyte formulation on degradation trends. In this context, a reduced-order representation focusing on the key differentiating species enables capturing the essential

physics, particularly the contrast between a flexible organic (LEDC-rich) SEI and a dense, passivating inorganic (LiF-rich) SEI. Previous FTIR (Fourier Transform Infrared Spectroscopy) and ToF-SIMS (Time-of-Flight Secondary Ion Mass Spectrometry) studies [38] have suggested the presence of oligomeric/polymeric species deriving from FEC. However, the quantitative contribution of such species to the total SEI mass and lithium consumption remains unclear. Therefore, these species were not explicitly incorporated into the present SEI model.

From NMR results (Figure 2), XPS results (Supporting Information S1), and the previous studies [32–34], we assumed three main reaction paths for the SEI growth

$$2\,EC + 2\,Li^+ + 2\,e^- \rightarrow LEDC + \text{gaseous product} \quad (1)$$

$$FEC + Li^+ + e^- \rightarrow LiF + \text{gaseous product} \quad (2)$$

$$PF_6^- + 3\,Li^+ + 2\,e^- \rightarrow 3\,LiF + \text{gaseous product} \quad (3)$$

In our model, the gaseous products are ignored to focus on the electrochemical performance impacted by solid products. Owing to the external pressure on the cell, it is assumed that gas products do not remain in the area where the electrodes face each other and do not induce additional degradations, such as contact resistance. We attempted an operando gas analysis for our cells with two electrolyte systems, but no gas was observed (Supporting Information S4). LEDC and LiF are the main SEI components treated in this article. A crude simplification in our treatment is to neglect the reaction of DMC into LMC, despite its large proportion in the total SEI weight, as evidenced by NMR (Figure 2). This assumption is motivated by the fact that DMC is present in all electrolyte systems investigated in this study and therefore acts as a common background solvent. In contrast, EC and FEC are the key differentiating components that determine the observed variations in SEI composition and electrochemical performance. As a result, the model is designed to explicitly capture the competition between EC-derived and FEC-derived reaction pathways, while DMC-related reactions are treated as a secondary contribution. We hypothesize that incorporating DMC decomposition would increase the overall lithium consumption in both electrolyte systems. Although the quantitative impact may differ depending on the degree of passivation and SEI evolution, the relative degradation trends are expected to remain primarily governed by the competition between EC-derived and FEC-derived SEI formation pathways. The omission of species such as DMC-derived products leads to an underestimation of the total lithium consumption. Based on the experimentally observed SEI composition, DMC-derived species constitute a non-negligible fraction of the experimentally observed SEI and may contribute significantly to lithium consumption. Therefore, the model may not fully capture the absolute magnitude of LLI, although the relative trends between electrolyte systems remain reasonably reproduced.

In addition to the electrochemical reduction pathway of PF_6^- in reaction (3), it should be noted that $LiPF_6$-based electrolytes are susceptible to hydrolysis in the presence of moisture, leading to the formation of HF and fluorophosphate species such as POF_3 and HPO_2F_2 [48, 49]. Such hydrolysis reactions are known to be accelerated under high-voltage conditions and can significantly influence interfacial chemistry. The generated HF is highly reactive and may alter SEI composition through reactions with carbonate-derived species, while also promoting transition-metal dissolution from the positive electrode. Although these parasitic reactions may affect the quantitative evolution of SEI components and degradation behavior, they are not explicitly included in the present model for simplicity.

Another important distinction from previous porous-SEI and crack-generation models, such as those proposed by Ekström and Lindbergh [50], is that the present work introduces component-specific mechanical responses associated with the large volume changes of SiO_x. While previous studies mainly discussed crack formation phenomenologically or in graphite-based systems, the present model separately describes the fracture/reformation of inorganic LiF-rich SEI and breathing-like thickness evolution of organic LEDC-rich SEI. LiF is easy to fracture when the SiO_x deforms during cycle aging, and the pores formed by the fracture can be a path for solvent transfer across the LiF layer. These pores can be filled by newly generated SEI products if a sufficient amount of reactants reaches the anode surface and the electrode potential is sufficiently low. This assumption is supported by previous studies [51, 52] showing that LiF is a mechanically stiff and brittle SEI component with a high elastic modulus, making it susceptible to fracture under large volume changes. It has also been reported that LiF loses its mechanical integrity during electrochemical cycling, undergoing structural breakdown. Such degradation is accompanied by a dynamic repair process, where the SEI is continuously reformed from electrolyte decomposition. Our model assumes that the fracture of LiF takes place at the end of the discharge process.

On the other hand, LEDC is considered an intrinsically porous SEI, which can change its thickness during cycle aging. To represent the afore-mentioned breathing behavior [41], continuously growing LEDC is forced to shrink down to the threshold thickness at the end of the discharge process. The behaviors of LiF and LEDC in our model are schematically illustrated in Figure 3.

The previously proposed porous-SEI continuum framework [24, 25] provided an important theoretical basis for describing SEI morphology and porosity evolution. However, these studies mainly focused on local SEI growth at the particle scale and did not explicitly connect experimentally quantified SEI chemistry with electrode-scale P2D degradation behavior. In contrast, the present work combines experimentally measured SEI compositions, reference-electrode electrochemical analyses, and P2D simulations within the same SiO_x-based cell system.

3.2.2 | *Model Formalism and SEI Parameters*

The coupling of electrolyte consumption and growth of SEI is described as follows. First, reactions (1)–(3) are generally expressed as

$$\alpha_n X + \beta_n Li^+ + \gamma_n e^- \rightarrow \delta_n SEI \quad (4)$$

where n is the label of reactions in Equations (1)–(3). From the electrochemical point of view, the volume of the product per area $V_{sei,n}$ is described by

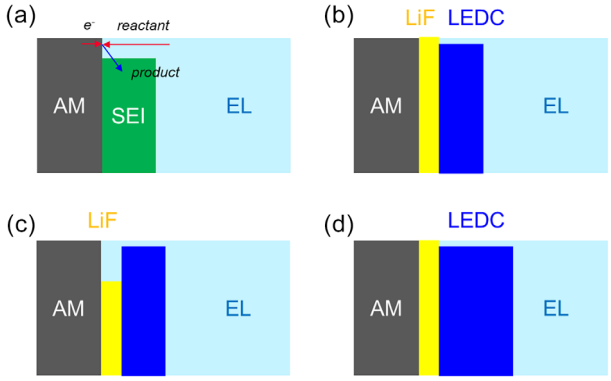

FIGURE 3 | (a) Porous SEI model. AM and EL represent active material and electrolyte, respectively. (b) Binary SEI model. (c) Inorganic SEI, LiF, has a specific thickness and a dynamic porosity during cycle aging. (d) Organic SEI, LEDC, has a specific porosity and a dynamic thickness during cycle aging.

$$\frac{\partial V_{sei,n}}{\partial t} = T_n \frac{M_{sei}}{\rho_{sei} F} \delta_n \tag{5}$$

where Tafel equation

$$T_n = -F k_{sei}^n \left(\frac{c_X}{c_X^0}\right)^{\alpha_n} \exp\left(-\gamma_n \frac{F}{2RT}(\eta_n - r_{sei} i_{SiOx})\right) \tag{6}$$

is considered to describe the solvent reduction kinetics for each reaction path. F and R are the Faraday and the gas constants and T is the temperature. k_{sei}^n is the kinetic constant of reaction n. c_X is the concentration of reactant X at the anode surface, whereas c_X^0 is its reference concentration. The overpotential η_n, related to the n^{th} reaction, depends on the SEI equilibrium potential value, denoted U_{sei}^n, as follows:

$$\eta_n = \Phi_s - \Phi_l - U_{sei}^n \tag{7}$$

where Φ_s and Φ_l are the electrochemical potentials in the active material and in the electrolyte, respectively.

Next, we look at the diffusion flux, mass flow of reactants, in the SEI. We assume that the reaction rate is limited by the diffusion of reactants through the SEI. The diffusion flux is expressed as a function of the reactant concentration in the electrolyte c_X^{bulk} as

$$D_{f,n} = \frac{(c_X^{bulk} - c_X)}{r_{diff}} F \tag{8}$$

where r_{diff} is the necessary time for reactants to cross the SEI and reach SiO_x particles. It can be written as a function of the thickness and the diffusivity of layers, e_{LiF} and $D_{LiF,cracks}$, for the LiF layer, e_{LEDC} and D_{LEDC} for the LEDC layer. Note that as the LiF layer is modeled as a dense layer, only the diffusion through the porosity ϵ_{LiF} of this layer is considered

$$r_{diff} = \frac{e_{LiF}}{D_{LiF,cracks}\ \epsilon_{LiF}} + \frac{e_{LEDC}}{D_{LEDC}} \tag{9}$$

The *LEDC* layer thickness evolution over time is given by

$$\frac{\partial e_{LEDC}}{\partial t} = T_1 \frac{M_{LEDC}}{\rho_{LEDC} F} \tag{10}$$

The overpotential η_{SiOx} is defined as the difference between the solid phase potential, the electrolyte potential, and the equilibrium potential of SiO_x. The intercalation current density i_{SiOx} is defined by

$$i_{SiOx} = i_{0,SiOx}\left[\exp\left(\frac{\alpha(\eta_{SiOx} - r_{sei} i_{SiOx})F}{RT}\right) - \exp\left(-\frac{(1-\alpha)(\eta_{SiOx} - r_{sei} i_{SiOx})F}{RT}\right)\right] \tag{11}$$

The thicknesses of the SEI layers lead to the evaluation of their resistance using

$$r_{sei} = \frac{e_{LiF}}{K_{LiF}} + \frac{e_{LEDC}}{K_{LEDC}} \tag{12}$$

where K_{LiF} and K_{LEDC} are the ionic conductivities of LiF and LEDC. The reaction rate T_n is obtained by equalizing the Tafel Equation (6) and the diffusion flux Equation (8) under the diffusion-limited assumptions.

Finally, the capacity loss induced by the SEI is obtained by quantifying the loss of cyclable lithium associated with each reaction. We introduce Q_{loss}^n the capacity loss associated with the n^{th} reaction and the total capacity loss Q_{loss} induced by all the reactions. By denoting the SiO_x surface area as S_a,

$$Q_{loss}^n = T_n \gamma_n S_a \tag{13}$$

$$Q_{loss} = \sum_n Q_{loss}^n \tag{14}$$

This capacity loss is referred to as LLI. The capacity retention in terms of LLI is described as

$$R_{LLI} = \frac{Q_0 - Q_{loss}}{Q_0} \tag{15}$$

by denoting the initial capacity as Q_0. The above models were developed on COMSOL Multiphysics [53].

The parameters related to solvent/Li consumption and SEI formation are shown in Table 3. It should be emphasized that the present parameter setting was not obtained through a formal global optimization or error-minimization procedure. Instead, the parameters were empirically assigned based on a combination of experimental observations, literature values, and physically reasonable assumptions, with the primary objective of reproducing the electrolyte-dependent degradation trends observed experimentally.

The reduction potentials for EC and FEC have been determined based on our previous study using cyclic voltammetry on the thin-film SiO_x electrode [41]. The amount of LiF in SEI of DMC + FEC (0.00329 mg per 1 mg of SiO_x; 1st cycle) is larger than that of EC + DMC (0.00084 mg per 1 mg of SiO_x; 1st cycle), as shown in Figure 2a, indicating that FEC plays an important role in producing LiF compared with $LiPF_6$. Therefore, we chose the reduction potential of PF_6 anion (0.75 V), lower than that of FEC (0.9 V).

The reaction constant for EC reduction was selected based on the previous physics-based SEI models [16], where values on the

order of 10^{-9} mol m^{-2} s^{-1} were discussed for carbonate reduction reactions. The reaction constant for FEC reduction was intentionally assigned to be smaller than that for EC reduction, despite the higher reduction potential of FEC. This choice was motivated by our previous NMR analyses on EC + FEC + DMC-based electrolytes, which indicated that EC-derived organic SEI species, such as LEDC, still remain even in FEC-containing systems. This observation suggests that FEC reduction alone does not immediately produce a fully passivating LiF-rich layer and that EC reduction can continue at lower potentials. In contrast, the reaction constant for PF_6^- reduction was set to a sufficiently small value so that LiF formation originating from PF_6^- decomposition would not prematurely suppress solvent reduction reactions through excessive passivation.

The diffusivities assigned to solvent transport through SEI pores were selected with reference to previous porous-SEI and phase-field studies reporting Li-ion diffusion coefficients ranging from approximately 10^{-20} to 10^{-16} m^2 s^{-1} in SEI [54, 55]. In the present work, slightly larger diffusivities were assigned to neutral solvent species than to Li ions, reflecting their weaker electrostatic interactions within the SEI environment. The ionic conductivity of the SEI layers was selected based on representative values reported in previous multimodal SEI models [16].

Sensitivity analyses for the most influential degradation parameters, including the threshold thickness of LEDC and the maximum crack ratio of LiF, are discussed in Supporting Information S5. These analyses confirm that the qualitative electrolyte-dependent degradation trends reproduced by the model remain robust over physically reasonable parameter ranges.

TABLE 3 | SEI-related parameters. k_{sei}^n, $e_{LEDC,threshold}$, and $\varepsilon_{LiF,max}$ are the main calibrated parameters so that the model can reproduce the potential curves obtained by experiment.

Parameter	Value
$M_{sei,1}$ | Molar mass of LEDC	0.16203 kg/mol
$M_{sei,2}$, $M_{sei,3}$ | Molar mass of LiF	0.025939 kg/mol
$\rho_{sei,1}$| Density of LEDC	1600 kg/m^3
$\rho_{sei,2}$, $\rho_{sei,3}$ | Density of LiF	12 640 kg/m^3
U_{sei}^1 | reductive potential	0.6 V
U_{sei}^2 | reductive potential	0.90 V
U_{sei}^3 | reductive potential	0.75 V
k_{sei}^1 | reaction constant	1.36×10^{-9} mol/(s·m^2)
k_{sei}^2 | reaction constant	1.36×10^{-12} mol/(s·m^2)
k_{sei}^3 | reaction constant	1.36×10^{-22} mol/(s·m^2)
$e_{LEDC,0}$ | LEDC initial thickness	1×10^{-10} m
$e_{LEDC,threshold}$ | LEDC thickness threshold	2×10^{-8} m
e_{LiF} | LiF thickness	2×10^{-9} m
$\varepsilon_{LiF,\max}$ | LiF max crack ratio	0.2
D_{LEDC} | diffusion of solvents through pores in LEDC	1×10^{-19} m^2/s
$D_{LiF,cracks}$ | diffusion of solvents through pores in LiF	5×10^{-15} m^2/s
K_{LiF}, K_{LEDC} | ionic conductivity in LiF and LEDC	5×10^{-6} S/m

3.3 | Model Analysis

Figures 4 and 5 represent the experimental and calculated potential versus capacity curves in the 1st loading test with different discharge rates for EC + DMC and DMC + FEC systems, respectively. Overall, potential profiles (not only cell potentials but also separated positive and negative electrode potentials) are similar between the measured and simulated results. One can notice that the potential curves of the positive electrode mostly overlap with each other, even though discharge rates differ. On the other hand, the negative electrode potential increase at the end of discharge depends strongly on C-rate and can limit the cell capacity. This quick increase of negative electrode potential at high C-rate may be related to the slowdown of Li-ion diffusivity and insertion kinetics of SiO_x at low stoichiometry that was introduced in Table 2. It is noticeable that the negative electrode seems to limit the cell performance during charge at 2 C due to its large overpotential in Figure S13(c) of Supporting Information S6. For improved performance at higher C-rate, it may be required to modify the SiO_x material so that it can avoid such a slowdown at the end of the discharge step. The potential curves of EC + DMC and DMC + FEC are mostly similar at the beginning of cycle aging in Figures 4 and 5. To be precise, the overpotential of the cell voltage at 2C discharge is larger in EC + DMC. The differences of overpotentials at 1 mAh between EC + DMC and DMC + FEC are 0.15 V in experiment and 0.03 V in simulation based on cell voltage. From the point of negative electrode potential, the differences of overpotentials at 1 mAh between the two systems are 0.16 V in experiment and 0.03 V in simulation. The model result underestimates the overpotential difference consistently derived from the negative electrodes. The NMR results (Figure 2) indicate that the EC + DMC system forms a thicker SEI, which may be correlated with increased interfacial resistance associated with thicker SEI formation. As a result, the discharge capacity at fifth cycle (2 C discharge) estimated by the model is larger in DMC + FEC (1.71 mAh) than that in EC + DMC (1.67 mAh), which is qualitatively consistent with the experimental result, 1.87 mAh for DMC + FEC and 1.42 mAh for EC + DMC. In Supporting Information S7, we show model results with no SEI growth mode. In this no-SEI scenario, EC + DMC and DMC + FEC would exhibit completely same capacity, indicating that SEI actually plays a crucial role in differentiating these two electrolyte systems.

The potential curves of the cell voltage, the positive electrode potential, and the negative electrode potential at the first loading test with different charging rates are shown in Figures S13 and S14 of Supporting Information S6. Again, the model results reproduce the qualitative difference depending on the charging C-rates observed in experiments. The potential curves measured with different discharge rates in the second loading test are depicted in Figures S15 and S16, while those with different charge rates are displayed in Figures S17 and S18. If SEI growth is ignored, the potential curves at second discharge loading test are the same as the ones at first discharge loading test shown in Figures S19b–e) of Supporting Information S7. If Figures S15 and

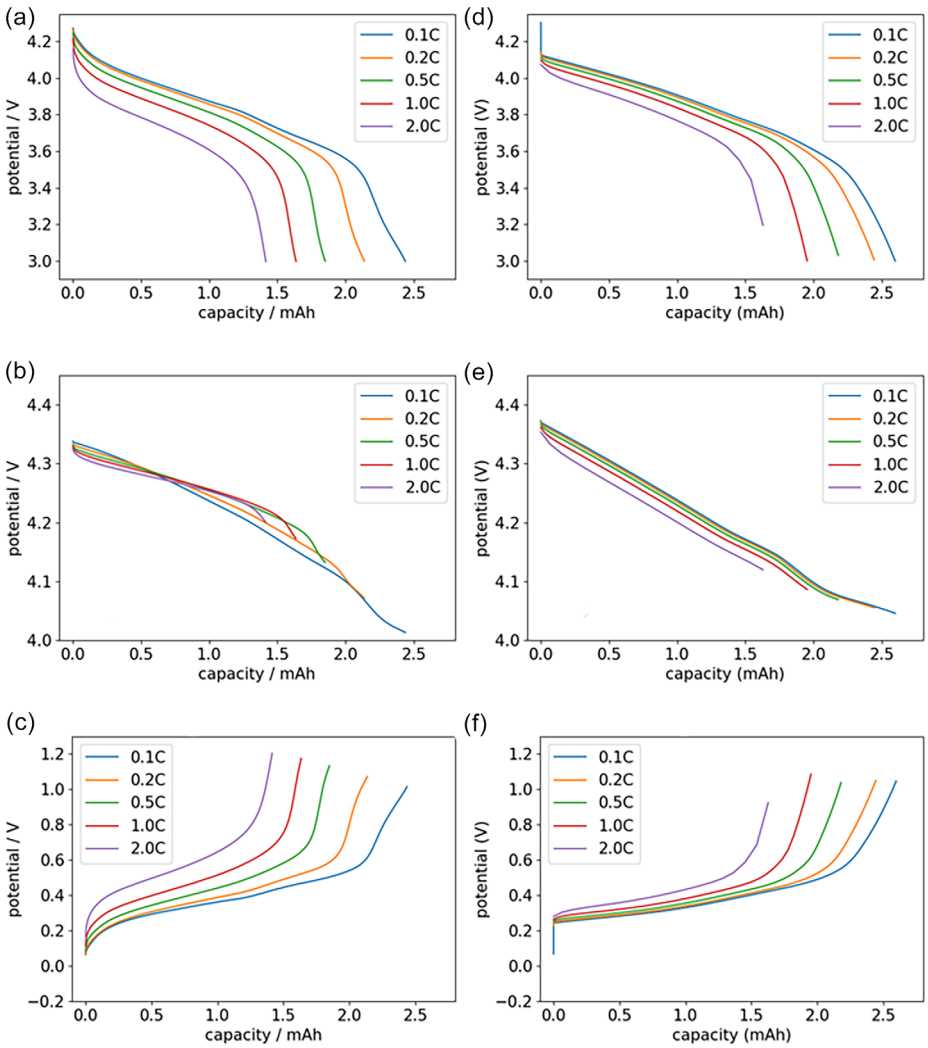

FIGURE 4 | Discharge potential-capacity (V-Q) curves for first loading tests depending on discharge C-rates for the EC + DMC system. Panels (a)–(c) show the experimental results, while panels (d)–(f) show the simulation results. Panels (a)–(d), panels (b)–(e), and panels (c)–(f) show cell potential, positive electrode potential, and negative electrode potential, respectively.

S16 are compared with the no-SEI scenario, it is clear that EC + DMC potentials show a significant modification by SEI, while DMC + FEC potentials maintain their initial appearance, indicating a relative stability. After aging, the consistency between experimental and simulated curves decreased compared with the results at the beginning of life. However, the qualitative trends by varying the discharge and charge rates are well reproduced in the model. Although some quantitative discrepancies remain between simulations and experiments, the model consistently captures the evolution of electrode overpotentials and available capacities.

In Figure 6, the discharge capacity retention estimated from the potential curves (potential vs. capacity, V-Q) and the discharge capacity retention in terms of LLI, determined by Equation (15), are plotted according to the model study. The capacity retentions at 100th cycle estimated by V-Q curves in the model are 65.1% and 96.8% for EC + DMC and DMC + FEC systems, respectively. The retentions at 100th cycle estimated by LLI in the model are 40.9% and 94.3% for the same two systems. Finally, experimentally observed capacity retentions at the 100th cycle are 25.5 and 61.2%, respectively, for EC + DMC and DMC + FEC. It should be noted that our cycle aging tests were conducted at 0.5C/0.5C condition as discussed in Section 2.1 to complete measurements within a reasonable experimental time, while we decided to carry out the model study of cycle aging tests at 0.1/0.1 C to account for the degradation in terms of LLI decoupled from the overpotential increase due to the SEI resistance. The overestimated capacity retention in the model may partially originate from the difference in C-rates or from the lack of detailed description in chemical reactions, where we assumed a simplified form as Equations (1)–(3).

The capacity retention by V-Q curves temporally decreases when the C-rate is high in the loading tests, but is recovered when the C-rate comes back to 0.1/0.1 C during cycle aging. Overall capacity retention for DMC + FEC exceeds that for EC + DMC, which is consistent with the experimental results shown in Figure 1. It is also shown that the capacity retention in terms of LLI is higher in DMC + FEC compared with EC + DMC, which again is in accordance with the experimental retention data. From an engineering perspective, such trend-level predictability is particularly

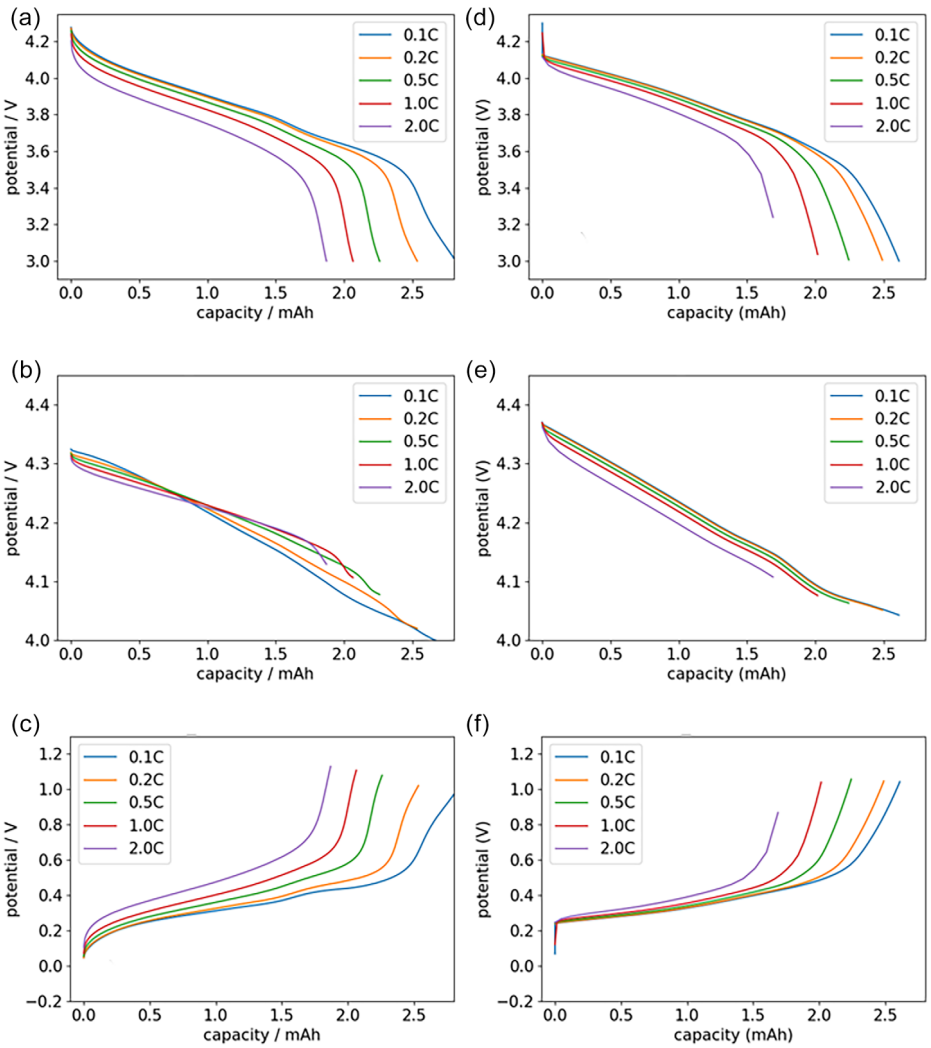

FIGURE 5 | Discharge potential-capacity (V-Q) curves for first loading tests depending on discharge C-rates for the DMC + FEC system. Panels (a)–(c) show the experimental results, while panels (d)–(f) show the simulation results. Panels (a)–(d), panels (b)–(e), and panels (c)–(f) show cell potential, positive electrode potential, and negative electrode potential, respectively.

valuable for degradation-oriented cell design, even when perfect quantitative agreement is not achieved.

For a clearer understanding of the model and its results, the status of SEI, namely the thickness of LEDC and the porosity of LiF, is plotted in Figure S20 of the Supporting Information S8 as a function of time in the early stages of aging tests. In EC + DMC, the LiF is almost always porous, while the thickness of LEDC periodically shifts since it was implemented as a breathing. In DMC + FEC, the LiF is the only SEI entity that is quickly recovered with the subsequent reactions even after it is damaged, which prevents further Li consumption.

In Figure 7, the negative electrode potentials at the end of rest after charge are plotted as a function of cycle number. Experimental results and simulation results show a qualitatively similar behavior, in which the negative electrode potential gradually increases with the cycle number, but the increase is slower in DMC + FEC. The reason for this shift of the negative electrode cutoff potential is twofold. First, due to the fast consumption of Li in the system, as evidenced by Figure 6b, the stoichiometry range used for charge/discharge has shifted in the anode active material. Second, although direct impedance measurements were not conducted in the present study, the gradual increase in negative electrode overpotential qualitatively suggests increasing interfacial resistance associated with SEI evolution. Future work, including impedance characterization, would further strengthen the interpretation of interfacial resistance evolution. The shift of the stoichiometry will be discussed further.

Figure 8 displays the spatial distribution of Li stoichiometry in the cathode and anode active materials at the end of discharge in the first and third loading tests (the loading tests inserted at first and 178th cycles as shown in Figure 1) in a P2D description. The horizontal axis indicates the position of the representative active material particle along the positive–negative electrode stacking direction, while the vertical axis indicates the distance from the surface of the representative active material particle. When the discharge rate is 0.1 C, the Li distributions in positive and negative electrodes are spatially homogeneous for both electrolytes. DMC + FEC shows a similar stoichiometry at the first and third loading tests, whereas the Li stoichiometry in LCO decreased after aging in EC + DMC. This is explained by the faster Li consumption due to the continuous SEI growth in EC + DMC.

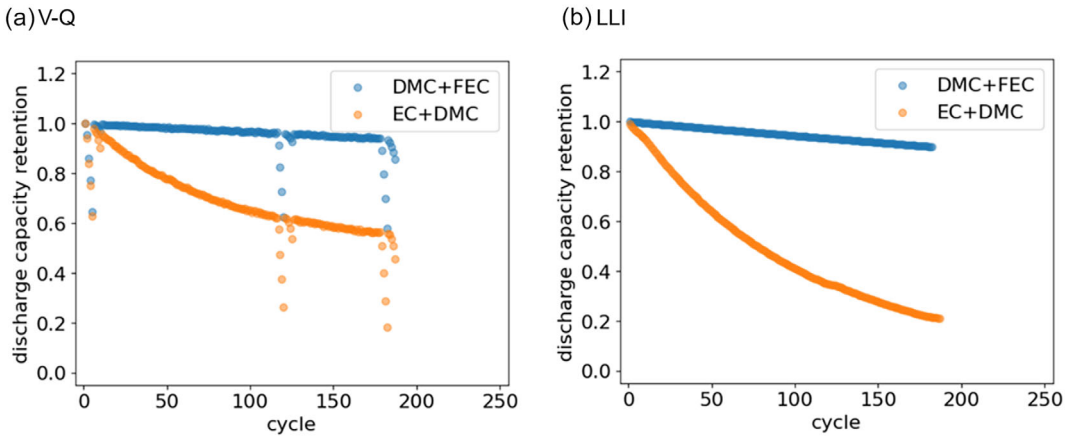

FIGURE 6 | Discharge capacity retention obtained by the developed P2D model. (a) Capacity estimated from the V–Q curves. (b) Capacity retention is estimated in terms of LLI.

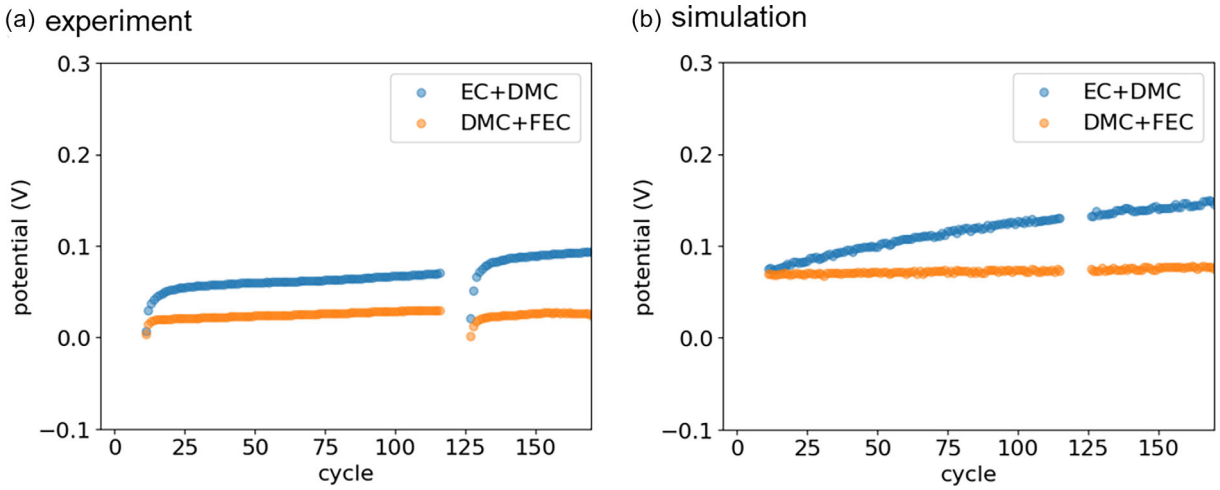

FIGURE 7 | Negative electrode potential at the end of rest time after charge as a function of cycle number. The data during the loading tests are excluded for simplicity. (a) Experiment. (b) Simulation. Blue and orange curves represent the data for EC + DMC and DMC + FEC, respectively.

When the discharge rate is 2 C, the distribution of Li is still homogeneous in the positive electrode, both at the first and third loading tests in both electrolyte systems. However, it can be mentioned that the stoichiometry of LCO after 2 C discharge is limited compared with 0.1 C, meaning that not all the Li is coming back to the cathode. On the other hand, the Li distribution in SiO_x shows a spatial inhomogeneity. This inhomogeneity in the anode is observed mostly along the particle radius, while it is mostly homogeneous in the depth of the electrode. This indicates that the Li near the SiO_x particle surface easily transfers to the electrolyte, but the Li located in the core of the particle cannot easily diffuse to the surface due to the slow dynamics of Li.

Figure 9 shows the spatial distribution of Li in active materials after charging of 1st and 3rd loading tests. Just after the 0.1 C charge, both electrodes show homogeneous Li distributions, though the stoichiometry in each electrode decreased after aging, significantly in EC + DMC and slightly in DMC + FEC. This result is consistent with the negative electrode potential shift observed in Figure 7.

After the 2 C charge, the Li distribution in LCO is still homogeneous in both electrolytes. Similar to the situation after the 2 C discharge, the Li distribution in SiO_x is again inhomogeneous in both electrolytes. However, there are a few differences worth discussing here. One is that the main direction of inhomogeneity is observed along the particle radius (vertical axis in the P2D description) at 2 C, but an inhomogeneity along the positive–negative electrode stacking direction (horizontal axis in the P2D description) also appears in both electrolytes. This is because the Li diffusivity in the liquid phase of the negative electrode is limited, and the Li ions in the electrolyte far from the separator are in deficit at high C-rate (the Li-ion concentration in the electrolyte is discussed in Supporting Information S9). To avoid this issue, improvement of electrolyte diffusivity and/or an improved electrolyte path geometry (higher porosity or lower tortuosity) in the negative electrode is desirable, especially when higher C-rate operation is demanded. A second interesting aspect is the relative stoichiometry in the negative electrode when two electrolytes are compared. Even at the first loading, the amount of Li inserted into SiO_x is lower in EC + DMC, because of the thicker SEI, which leads to a larger overpotential. After aging, the Li stoichiometry in SiO_x shows a similar gradation as the one observed at the beginning of life, but with a lower total Li content in SiO_x.

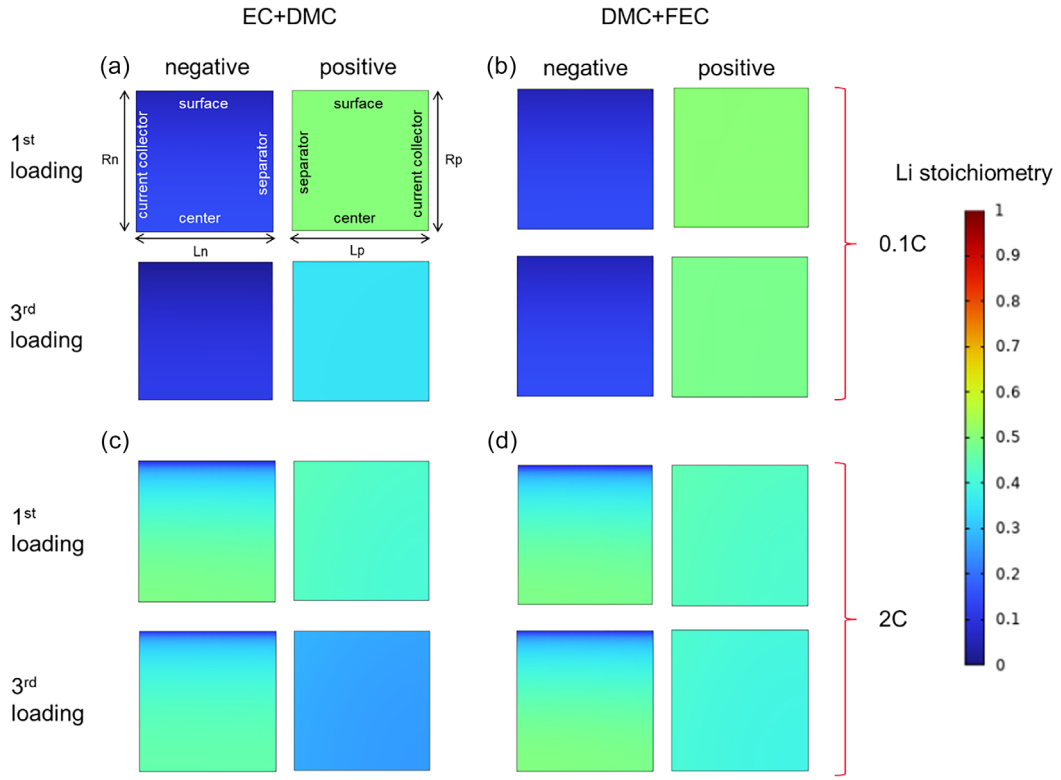

FIGURE 8 | Stoichiometry distribution in the electrodes at the end of first and third discharge loading tests. Negative electrode is described by a scaled square with a width of Ln = 12.5 µm (thickness of the negative electrode) and a height of Rn = 2.95 µm (mean particle radius of SiO_x), whereas positive electrode is described by a scaled square with a width of Lp = 51.6 µm (thickness of the positive electrode) and a height of Rp = 10.25 µm (mean particle radius of LCO). The geometry fully reflects the experimental setup. The upper side of the horizontal edge indicates the particle surface facing the electrolyte while the lower edge indicates the particle center of the active material. (a) EC + DMC and (b) DMC + FEC after 0.1 C discharge. (c) EC + DMC and (d) DMC + FEC after 2 C discharge.

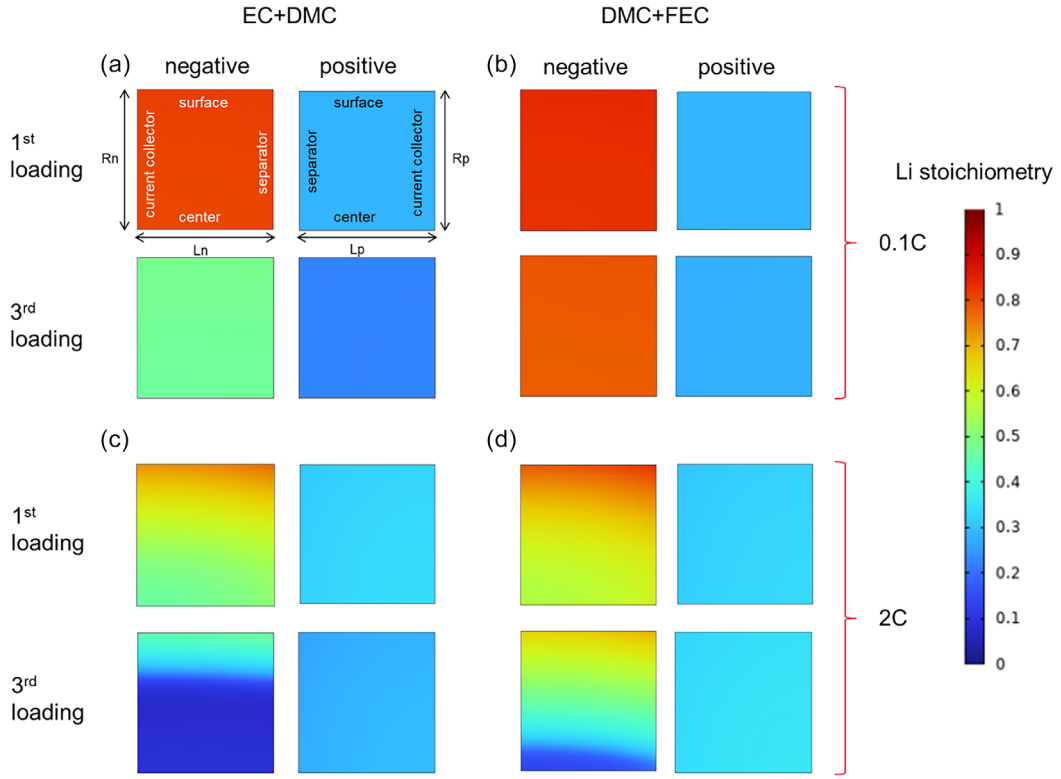

FIGURE 9 | Stoichiometry distribution in the electrodes at the end of first and third charge loading tests. Details of the expression are explained in the caption of Figure 8. (a) EC + DMC and (b) DMC + FEC after 0.1 C charge. (c) EC + DMC and (d) DMC + FEC after 2 C charge.

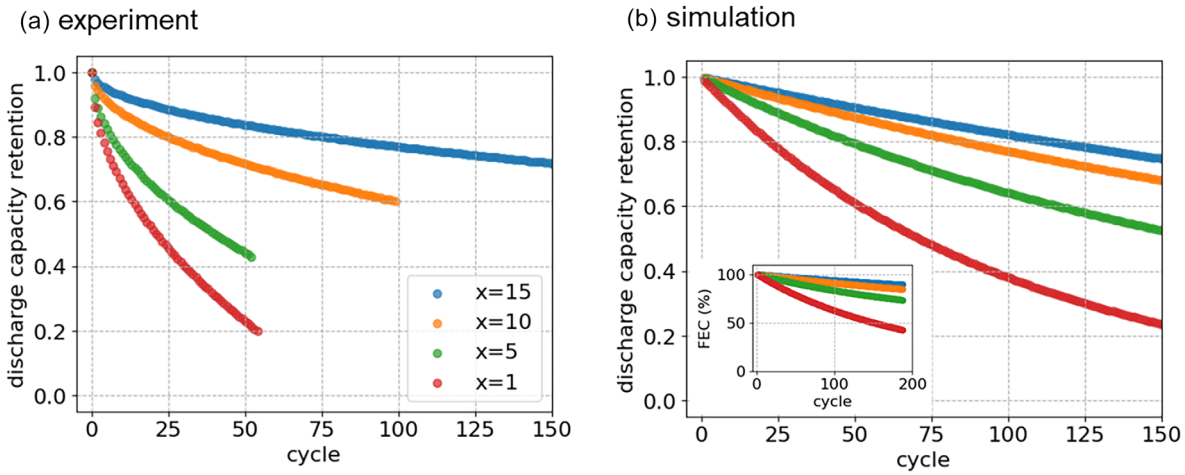

FIGURE 10 | Cycle aging tests for LCO|SiO_x cells using electrolytes with the following compositions: 1 M $LiPF_6$/EC + DMC + FEC, where EC:DMC:FEC = 15:85-x:x (wt%) with $x = 15$ (blue), $x = 10$ (orange), $x = 5$ (green) and $x = 1$ (red). (a) Experiment (0.5/0.5 C). (b) Simulated capacity retention from the LLI point of view. Simulations were conducted at 0.1/0.1 C. The inset shows the remaining FEC in the electrolyte as a function of cycle.

Finally, we applied the developed model to electrolytes mixed with three solvent species: 1 M $LiPF_6$/EC + DMC + FEC. Figure 10a displays the experimental cycle aging tests for 1 M $LiPF_6$/EC + DMC + FEC, where the EC ratio was fixed to 15%, and the FEC ratio was changed from 1 to 15%. The corresponding model results were illustrated in Figure 10b. In our experimental study, the initial slope of discharge capacity retention varies depending on the FEC ratio, which was well reproduced by the developed model. The capacity retentions at 50th cycle observed in experiment are 82%, 72%, 43%, and 22% for 15%, 10%, 5%, and 1% contents of FEC, respectively, while those estimated by the developed model are 91%, 86%, 80%, and 60%. A quantitative agreement is not perfect, but the trend in the degree of degradation as a function of FEC content is reproduced by the model. These agreements support the wide applicability of the model for $LiPF_6$/EC + DMC + FEC systems. The inset of Figure 10b shows the remaining amount of FEC in the electrolyte as a function of cycle. FEC decreases gradually and nonlinearly, a behavior that is quite similar to that of capacity retention. This indicates a close relationship between the consumption of solvents and Li and the SEI growth embedded in our model. In the currently developed model, the electrolyte composition changes as SEI recursively forms, which in turn modifies the SEI formation process, synergetically affecting the cell performance. Incorporating the change of electrolyte properties, such as ion conductivity, depending on modified electrolyte composition, would be an interesting subject for future studies. Observations when some of the species in the electrolyte are fully consumed would also be an interesting topic.

The present binary SEI representation does not explicitly account for the full spectrum of inorganic and organic species reported in Si-based systems. While such ignored species may affect properties such as ionic conductivity, mechanical stability, and long-term SEI evolution, their omission can be interpreted as a source of quantitative deviation to the present model in terms of lithium consumption and does not alter the qualitative trends captured in this study. Incorporating a more detailed multicomponent SEI description and its detailed sensitivity analysis will be addressed in future work to improve the predictive capability of the model.

4 | Conclusion

In this study, we systematically investigated the effects of electrolyte composition on cycle retention, SEI characteristics, and LLI in SiO_x-based negative electrodes, combining experimental analysis and physics-based modeling.

Electrochemical cycling results clearly demonstrated that electrolytes containing FEC exhibit superior cycle retention compared to conventional EC + DMC systems. In particular, DMC + FEC showed improved capacity retention, indicating a beneficial role of FEC in suppressing degradation during cycling. Additional cycle aging tests using ternary $LiPF_6$/EC + DMC + FEC electrolytes further revealed that reducing the FEC content leads to accelerated degradation, as evidenced by a steeper decline in capacity retention even at the beginning of life. This result highlights the critical role of FEC in the initial formation and stabilization of the SEI.

NMR analyses revealed that LEDC and LiF are the key SEI components responsible for the distinct interfacial properties observed in EC + DMC and DMC + FEC electrolytes. The SEI formed in DMC + FEC is characterized by a thinner and LiF-rich structure. Notably, the total SEI mass remained nearly constant even after aging, qualitatively suggesting a "breathing" behavior of the SEI, where reversible structural changes occur without continuous accumulation.

Based on SEI quantification results, we developed a P2D model that couples electrolyte consumption with SEI growth using a porous SEI framework. For simplicity, degradation reactions were effectively imposed on EC, FEC, and the PF_6 anion, while DMC was neglected. In the model, inorganic SEI components such as LiF, originating from FEC and PF_6 decomposition, were represented as a thin but brittle film, whereas organic SEI components such as LEDC, originating from EC, were modeled as a breathing entity. This treatment successfully reproduced a lower negative electrode overpotential in the DMC + FEC system, consistent with the formation of a thinner, LiF-rich SEI. Furthermore, the simulated LLI successfully captured the experimentally observed capacity-fade trends.

Continuous SEI formation consumes cyclable lithium and limits the usable stoichiometry range during charge and discharge. Our results indicate that lithium consumption is relatively suppressed in DMC + FEC, most likely due to more effective passivation by the LiF-rich SEI, leading to improved cycling stability.

The developed P2D model also provides insights into the spatial inhomogeneity of lithium distribution within the cell. Analysis of lithium stoichiometry revealed that inhomogeneity predominantly occurs in the negative electrode rather than in the positive electrode, which is attributed to the slow lithium transport kinetics in SiO_x particles. After high-rate discharging at 2 C, lithium inhomogeneity was mainly observed along the particle radial direction. This suggests that further improvement of SiO_x, such as through atomic doping [56], control of disproportionation via thermal treatment [57–59], or fine-tuning of particle size, is essential for fast discharge applications. In contrast, 2C charging induced inhomogeneity not only along the particle radius but also across the electrode thickness, indicating that limited lithium transport in the electrolyte also plays a significant role. Therefore, enhancing electrolyte properties and optimizing electrolyte pathway topology are required to achieve faster and more homogeneous charging.

The degradation behaviors reproduced by the present model are broadly consistent with experimentally reported characteristics of Si-based and SiO_x-based electrodes. The model captures key features widely discussed in previous studies, including the formation of LiF-rich passivating SEI in FEC-containing electrolytes, continuous lithium consumption associated with recurrent SEI reformation, and the dynamic evolution of the interphase during cycling [8–11, 38–44]. These consistencies support the physical relevance of the present chemistry-informed degradation framework and suggest that the model provides a useful tool for interpreting the coupled relationships between electrolyte composition, SEI chemistry, lithium consumption, and electrochemical aging in SiO_x-based cells. This approach goes beyond conventional phenomenological SEI growth models and provides a practical methodology for connecting SEI characterization, electrolyte formulation, and long-term electrochemical degradation. By coupling electrochemical and degradation models, the framework provides a rough yet valuable estimation of battery lifetime, which would otherwise require long-term experiments. Future work will focus on validating the model under different temperature conditions and extending it to even higher charge/discharge C-rates to accelerate the design of advanced high-performance LIBs. Specifically to validate the model's ability at different temperatures, it is of interest to incorporate temperature dependency into the diffusivity of reactants across the SEI pore D_{sei}, ionic conductivity in SEI K_{sei}, or the threshold thickness of organic SEI $e_{LEDC,threshold}$. Further improvements of the model will include the incorporation of additional SEI components to capture the full chemical complexity and enhance quantitative accuracy. In particular, incorporating DMC decomposition reactions would improve the quantitative prediction of lithium consumption, even though it is not expected to significantly modify the electrolyte-dependent trends discussed in this study. Complementary characterization by ToF-SIMS and FTIR will clarify the possible contribution of oligomeric and polymeric SEI species derived from FEC decomposition, which would upgrade the model description. It could also be a promising research direction to apply and extend the developed model to other batteries with different types of silicon anodes, such as silicon-metal alloys and pure silicon.

Acknowledgments

The authors acknowledge Ms. Akari Nagashima (Murata Manufacturing Co., Ltd.) for her support on the NMR measurements. The authors appreciate the discussions with Ms. Aiko Kanazawa (Murata Manufacturing Co., Ltd.) regarding the experimental techniques. We also thank Dr. Marion Chandesris (CEA, LITEN) for the useful discussions.

Open access publication funding provided by COUPERIN CY26.

Conflicts of Interest

The authors declare no conflicts of interest.

Data Availability Statement

The data that support the findings of this study are available from the corresponding author upon reasonable request.

References

1. G. Zubi, R. Dufo-López, M. Carvalho, and G. Pasaoglu, "The Lithium-Ion Battery: State of the Art and Future Perspectives," *Renewable and Sustainable Energy Reviews* 89 (2018): 292.

2. M. Rahimi, "Lithium-Ion Batteries: Latest Advances and Prospects," *Batteries* 7 (2021): 8.

3. M. S. Ramkumar, C. S. R. Reddy, A. Ramakrishnan, et al., "Review on Li-Ion Battery with Battery Management System in Electrical Vehicle," *Advances in Materials Science and Engineering* 2022 (2022): 3379574.

4. Z. Liu, Q. Yu, Y. Zhao, et al., "Silicon Oxides: A Promising Family of Anode Materials Rfor Lithium-Ion Batteries," *Chemical Society Reviews* 48 (2019): 285.

5. K. Kitada, O. Pecher, P. C. M. M. Magusin, M. F. Groh, R. S. Weatherup, and C. P. Grey, "Unraveling the Reaction Mechanisms of SiO Anodes for Li-Ion Batteries by Combining In Situ ^{7}Li and Ex Situ ^{7}Li/^{29}Si Solid-State NMR Spectroscopy," *Journal of the American Chemical Society* 141 (2019): 7014.

6. X. Zhou, Z. Qi, Q. Liu, et al., "Research Progress of Silicon Suboxide-Based Anodes for Lithium-Ion Batteries," *Frontiers in Materials* 7 (2021): 628233.

7. Y. Yang, Y. Liu, X. Jiang, L. Zhao, P. Wang, and Y. Zhang, "Rational Design of SiO_x Based Anode Materials for Next Generation Lithium-Ion Batteries," *Materials Advances* 5 (2024): 896.

8. R. Jung, M. Metzger, D. Haering, et al., "Consumption of Fluoroethylene Carbonate (FEC) on Si-C Composite Electrodes for Li-Ion Batteries," *Journal of the Electrochemical Society* 163 (2016): A1705.

9. Y. Li, Z. Cao, Y. Wang, et al., "New Insight into the Role of Fluoro-Ethylene Carbonate in Suppressing Li-Trapping for Si Anodes in Lithium-Ion Batteries," *ACS Energy Letters* 8 (2023): 4193.

10. C. C. Nguyen and B. L. Lucht, "Comparative Study of Fluoroethylene Carbonate and Vinylene Carbonate for Silicon Anodes in Lithium-Ion Batteries," *Journal of the Electrochemical Society* 161 (2014): A1933.

11. Y. Jin, N.-J. H. Kneusels, P. C. M. M. Magusin, et al., "Identifying the Structural Basis for the Increased Stability of the Solid Electrolyte Interphase Formed on Silicon with the Additive Fluoroethylene Carbonate," *Journal of the American Chemical Society* 139 (2017): 14992.

12. M. Doyle, T. F. Fuller, and J. Newman, "Modeling of Galvanostatic Charge and Discharge of the Lithium/Polymer/Insertion Cell," *Journal of the Electrochemical Society* 140 (1993): 1526.

13. S. G. Marquis, R. Timms, V. Sulzer, C. P. Please, and S. J. Chapman, "A Suite of Reduced-Order Models of a Single-Layer Lithium-Ion Pouch Cell," *Journal of the Electrochemical Society* 167 (2020): 140513.

14. F. B. Planella, W. Ai, A. M. Boyce, et al., "A Continuum of Physics-Based Lithium-Ion Battery Models Reviewed," *Progress in Energy* 4 (2022): 042003.

15. M. Mama, E. Solai, T. Capurso, A. Danlos, and S. Khelladi, "Comprehensive Review of Multi-Scale Lithium-Ion Battery Modeling: From Electro-Chemical Dynamics up to Heat Transfer in Battery Thermal Management System," *Energy Conversion and Management* 325 (2025): 119223.

16. M. Safari, M. Morcrette, A. Teyssot, and C. Delacourt, "Multimodal Physics-Based Aging Model for Life Prediction of Li-Ion Batteries," *Journal of the Electrochemical Society* 156 (2009): A145.

17. J. M. Reniers, G. Mulder, and D. A. Howey, "Review and Performance Comparison of Mechanical-Chemical Degradation Models for Lithium-Ion Batteries," *Journal of the Electrochemical Society* 166 (2019): A3189.

18. S. E. J. O'Kane, W. Ai, G. Madabattula, et al., "Lithium-Ion Battery Degradation: How to Model It," *Physical Chemistry Chemical Physics* 24 (2022): 7909.

19. M. Zhuo, G. Offer, and M. Marinescu, "Degradation Model of High-Nickel Positive Electrodes: Effects of Loss of Active Material and Cyclable Lithium on Capacity Fade," *Journal of Power Sources* 556 (2023): 232461.

20. P. Ramadass, B. Haran, P. M. Gomadam, R. White, and B. N. Popov, "Development of First Principles Capacity Fade Model for Li-Ion Cells," *Journal of the Electrochemical Society* 151 (2004): A196.

21. M. B. Pinson and M. Z. Bazant, "Theory of SEI Formation in Rechargeable Batteries: Capacity Fade, Accelerated Aging and Lifetime Prediction," *Journal of the Electrochemical Society* 160 (2012): A243.

22. M. Tang, S. Lu, and J. Newman, "Experimental and Theoretical Investigation of Solid-Electrolyte-Interphase Formation Mechanisms on Glassy Carbon," *Journal of the Electrochemical Society* 159 (2012): A1775.

23. D. Li, D. Danilov, Z. Zhang, H. Chen, Y. Yang, and P. H. L. Notten, "Modeling the SEI-Formation on Graphite Electrodes in $LiFePO_4$ Batteries," *Journal of the Electrochemical Society* 162 (2015): A858.

24. B. Horstmann, F. Single, and A. Latz, "Review on Multi-Scale Models of Solid-Electrolyte Interphase Formation," *Current Opinion in Electrochemistry* 13 (2019): 61.

25. F. Single, B. Horstmann, and A. Latz, "Revealing SEI Morphology: In-Depth Analysis of a Modeling Approach," *Journal of the Electrochemical Society* 164 (2017): E3132.

26. G. Qian, Y. Li, H. Chen, et al., "Revealing the Aging Process of Solid Electrolyte Interphase on SiOx Anode," *Nature Communications* 14 (2023): 6048.

27. Y. J. Choi, J.-Y. Bae, G.-O. Park, and S.-H. Yu, "Degradation Pathways of Silicon-Based Anodes in Lithium-Ion Batteries," *Advanced Energy Materials* 16 (2026): e06750.

28. M. S. Whittingham, "Lithium Batteries and Cathode Materials," *Chemical Reviews* 104 (2004): 4271.

29. J. H. Zhang, Y. H. Jin, J. B. Liu, Q. Q. Zhang, and H. Wang, "Recent Advances in Understanding and Relieving Capacity Decay of Lithium Ion Batteries with Layered Ternary Cathodes," *Sustainable Energy & Fuels* 5 (2021): 5114.

30. E. C. Cengiz, J. Rizell, M. Sadd, A. Matic, and N. Mozhzhukhina, "Review-Reference Electrodes in Li-Ion and Next Generation Batteries: Correct Potential Assessment, Applications and Practices," *Journal of the Electrochemical Society* 168 (2021): 120539.

31. J. P. Allen and C. P. Grey, "Solution NMR of Battery Electrolytes: Assessing and Mitigating Spectral Broadening Caused by Transition Metal Dissolution," *The Journal of Physical Chemistry C* 127 (2023): 4425.

32. Y. Wang, S. Nakamura, M. Ue, and P. B. Balbuena, "Theoretical Studies to Understand Surface Chemistry on Carbon Anodes for Lithium-Ion Batteries: Reduction Mechanisms of Ethylene Carbonate," *Journal of the American Chemical Society* 123 (2001): 11708.

33. Y. Wang and P. B. Balbuena, "Theoretical Studies on Cosolvation of Li Ion and Solvent Reductive Decomposition in Binary Mixtures of Aliphatic Carbonates," *International Journal of Quantum Chemistry* 102 (2005): 724.

34. U. Purushotham, N. Takenaka, and M. Nagaoka, "Additive Effect of Fluoroethylene and Difluoroethylene Carbonates for Solid Electrolyte Interphase Film Formation in Sodium-Ion Batteries: A Quantum Chemical Study," *RSC Advances* 6 (2016): 65232.

35. R. Lundström, N. Gogoi, T. Melin, and E. J. Berg, "Unveiling Reaction Pathways of Ethylene Carbonate and Vinylene Carbonate in Li-Ion Batteries," *The Journal of Physical Chemistry C* 128 (2024): 8147.

36. M. Nie, J. Demeaux, B. T. Young, et al., "Effect of Vinylene Carbonate and Fluoroethylene Carbonate on SEI Formation on Graphitic Anodes in Li-Ion Batteries," *Journal of the Electrochemical Society* 162 (2015): A7008.

37. K. U. Schwenke, S. Solchenbach, J. Demeaux, B. L. Lucht, and H. A. Gasteiger, "The Impact of CO_2 Evolved From VC and FEC during Formation of Graphite Anodes in Lithium-Ion Batteries," *Journal of the Electrochemical Society* 166 (2019): A2035.

38. S. Barua, D. P. Abraham, and K. P. C. Yao, "On the Dynamics of the Fluoroethylene Carbonate Generated Solid Electrolyte Interphase on Silicon Anodes during Calendar Life Aging," *Electrochimica Acta* 535 (2025): 146624.

39. J. Tan, J. Matz, P. Dong, J. Shen, and M. Ye, "A Growing Appreciation for the Role of LiF in the Solid Electrolyte Interphase," *Advanced Energy Materials* 11 (2021): 2100046.

40. F. Jiang, Y. Sun, K. Zhang, Y. Liu, X. Feng, and H. Xiang, "SiOx/C Anodes with High Initial Coulombic Efficiency through the Synergy Effect of Pre-Lithiation and Fluoroethylene Carbonate for Lithium-Ion Batteries," *Electrochimica Acta* 398 (2021): 139315.

41. Z. Lu, K. Zrikem, F. L. Cras, et al., "Probing Surface Dynamics of SiO_x Thin-Film Electrodes during Cycling through X-Ray Photoemission Spectroscopy and Operando X-Ray Reflectivity," *ACS Applied Materials & Interfaces* 16 (2024): 52130.

42. Z. Zhuo, P. Lu, C. Delacourt, et al., "Breathing and Oscillating Growth of Solid-Electrolyte-Interphase upon Electrochemical Cycling," *Chemical Communications* 54 (2018): 814.

43. T. M. Fears, M. Doucet, J. F. Browning, et al., "Evaluating the Solid Electrolyte Interphase Formed on Silicon Electrodes: A Comparison of Ex Situ X-Ray Photoelectron Spectroscopy and In Situ Neutron Reflectometry," *Physical Chemistry Chemical Physics* 18 (2016): 13927.

44. I. Hasa, A. M. Haregewoin, L. Zhang, et al., "Electrochemical Reactivity and Passivation of Silicon Thin-Film Electrodes in Organic Carbonate Electrolytes," *ACS Applied Materials & Interfaces* 12 (2020): 40879.

45. E. Sivonxay, M. Aykol, and K. A. Persson, "The Lithiation Process and Li Diffusion in Amorphous SiO_2 and Si From First Principles," *Electrochimica Acta* 331 (2020): 135344.

46. K. Xu, "Electrolytes and Interphases in Li-Ion Batteries and beyond," *Chemical Reviews* 114 (2014): 11503.

47. S. Saleh, S. Daboss, T. Philipp, D. Schäfer, M. Rohnke, and C. Kranz, "Probing the Properties of Locally Formed Solid Electrolyte Interphases on Hard Carbon Anodes," *ChemElectroChem* 12 (2025): e202400707.

48. M. Stich, M. Göttlinger, M. Kurniawan, U. Schmidt, and A. Bund, "Hydrolysis of $LiPF_6$ in Carbonate-Based Electrolytes for Lithium-Ion

Batteries and in Aqueous Media," *The Journal of Physical Chemistry C* 122 (2018): 8836.

49. M. Liu, J. Vatamanu, X. Chen, L. Xing, K. Xu, and W. Li, "Hydrolysis of $LiPF_6$-Containing Electrolyte at High Voltage," *ACS Energy Letters* 6 (2021): 2096.

50. H. Ekström and G. Lindbergh, "A Model for Predicting Capacity Fade due to SEI Formation in a Commercial Graphite/$LiFePO_4$ Cell," *Journal of the Electrochemical Society* 162 (2015): A1003.

51. H. Shin, J. Park, S. Han, A. M. Sastry, and W. Lu, "Component-/Structure-Dependent Elasticity of Solid Electrolyte Interphase Layer in Li-Ion Batteries: Experimental and Computational Studies," *Journal of Power Sources* 277 (2015): 169.

52. M. He, R. Guo, G. M. Hobold, H. Gao, and B. M. Gallant, "The Intrinsic Behavior of Lithium Fluoride in Solid Electrolyte Interphases on Lithium," *Proceedings of the National Academy of Sciences* 117 (2020): 73.

53. *COMSOL Multiphysics v. 6.0* (2021, COMSOL AB), http://www.comsol.com.

54. N. Kamyab, J. W. Weidner, and R. E. White, "Mixed Mode Growth Model for the Solid Electrolyte Interface (SEI)," *Journal of the Electrochemical Society* 166 (2019): A334.

55. P. Guan and L. Liu, "Lithium-Ion Diffusion in Solid Electrolyte Interface (SEI) Predicted by Phase Field Model," *MRS Proceedings* 1753 (2015): 31–37.

56. T. Kim, H. Li, R. Gervasone, J. M. Kim, and J. Y. Lee, "Review on Improving the Performance of SiO_x Anodes for a Lithium-Ion Battery through Insertion of Heteroatoms: State of the Art and Outlook," *Energy & Fuels* 37 (2023): 13563.

57. B.-C. Yu, Y. Hwa, J.-H. Kim, and H.-J. Sohn, "A New Approach to Synthesis of Porous SiO_x Anode for Li-Ion Batteries via Chemical Etching of Si Crystallites," *Electrochimica Acta* 117 (2014): 426.

58. K. Yasuda, Y. Kashitani, S. Kizaki, K. Takeshita, T. Fujita, and S. Shimosaki, "Thermodynamic Analysis and Effect of Crystallinity for Silicon Monoxide Negative Electrode for Lithium-Ion Batteries," *Journal of Power Sources* 329 (2016): 462.

59. Y. Cao, R. A. Dunlap, and M. N. Obrovac, "Electrochemistry and Thermal Behavior of SiO_x Made by Reactive Gas Milling," *Journal of the Electrochemical Society* 167 (2020): 110501.

Supporting Information

Additional supporting information can be found online in the Supporting Information section.